Rijks*universiteit* Groningen

Faculteit der Wiskunde en Natuurkunde, Zernike Institute for Advanced Materials

Onderzoeksgroep: Fysica van Nanodevices

Spin dephasing of electron ensembles in epitaxial bulk GaAs materials:

Crystal-orientation dependant dephasing in wires and observation of unexpected values of the Landé g-factor

Master thesis by:

Andrii Rudavskyi

Group Leader: Prof. Dr. Ir. B.J. van Wees

Supervisors: Prof. Dr. Ir. C.H. van der Wal,
Msc. S.Z. Denega

Referent: Prof. Dr. Ir. P.H.M. van Loosdrecht

Period: September 2008 – September 2009

Credits: 54 ECTS

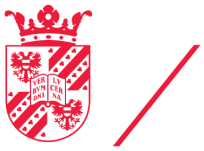

rijksuniversiteit groningen

Abstract

Inhomogeneous spin-dephasing due to spin-orbit interaction is one of the processes that cause loss of the average spin orientation of the spin system. To be able to control spin dephasing would be of great benefit for further development of spintronic devices. One of the ways to implement this is to make ballistic confinement of quasi-free electron gas in directions of high spin-orbits field. Both numerical and experimental studies have shown that confinement of 2DEG to quasi one dimensional wires lead to anisotropy of the spin dephasing time, thus strongly suppressing spin dephasing for [110] wire orientation. In thesis we present numerical simulations that show that such anisotropy for spin dephasing can also occur for wires with a bulk electron ensemble (3DEG). These results provide a first model for the unexpected observation of spin dephasing anisotropy for bulk GaAs layers in recent experiments by our team. We use a Monte-Carlo approach in which electrons are modeled as particles that are ballistically confined in two directions while they can freely move along the direction of a wire.

In the second part of the thesis TRKR measurements of the spin dephasing in n-GaAs were performed. Spin-dephasing time and g-factor dependence on pump power was retrieved from the experimental data. It is shown that g-factor exhibits drift toward higher absolute values during experiment for high pump intensities and that it is a consequence of band filling effects. Unexpected value of the g-factor (0.483) was observed at low pump intensities.

Table of content

1 Introduction

One of the most remarkable inventions of the past century was transistor. This opened era of solid state electronics, transistor becoming the basic element of it. With the advances of the present-day lithographic techniques it became possible to reduce size of these devices and thus to achieve high levels of integration. For example, the size of the transistor on commercially fabricated chip has reached 45 nm. Not only these trends in technology led to miniaturization of old, well known devices, such as field effect transistor, but also to design and fabrication of a principally new nanodevices, which exploit quantum effects as a basis for their functionality.

Despite this contemporary focus on semiconductor quantum devises, a principal quantum mechanical aspect of electron – its spin has largely been neglected. In recent years, however, new ideas of how to use this additional electron's degree of freedom have shown up. This new field of physics which studies properties of electron's spin in combination with its charge is called spintronics or magnetoelectronics.

Although early research on spin-polarized transport trace back to pioneering works of Mott in 1930s the real implementation of spin-dependent phenomena became possible only after discovery of the giant magnetoresistance effect (GMR) in 1988 [1][1]. This effect occurs in thin film layered structures with alternating ferromagnetic and nonmagnetic layers and manifests itself in strong dependence of the resistivity of the film on the relative orientation of the magnetization of each ferromagnetic layer. Nowadays giant magnetoresistance effect lies at the heart of computer hard disk drive operation.

In order to successfully design spintronic device one should be able to solve problems of spin injection and detection. Both injection and detection can be realized by electrical and optical methods [2]. Another important question that one faces when dealing with spintronics is how long does the spin live? In other words, how long can system keep it spin orientation and which processes cause loss of this spin orientation? In the systems we are going to investigate these processes mainly occur due to spin-dephasing by spin-orbit fields.

Time resolved Kerr rotation (TRKR) technique is an important experimental tool to investigate time evolution of the spin orientation inside of a crystal. In this technique, a non-equilibrium spin population is initially excited by pump laser pulse. Then time evolution of this population is traced with the help of delayed in time probe pulse. Thus by looking at the relaxation of the Kerr signal in time we can get an insight of how spins are dephasing inside of a crystal.

The goal of this project is to study spin dephasing of spin ensembles in GaAs systems. It consists of two parts: 1) Numerical simulations of the spin dephasing of 3D spin ensembles that are balistically confined to quasi 1D wire. 2) Experimental measurements of the spin-dephasing in n-GaAs system by means of TRKR.

A motivation for numerical simulations came from two works [5], [6]. In [5] it was shown numerically that there exists anisotropy of spin dephasing time for 2DEG spin system that is ballistically confined to quasi 1D wire. On the other hand authors of [6] experimentally studied spin dephasing in 2DEG structures with etched wires on the surface. Interestingly, they observed superposition of two Kerr signals, both of which

[1] Albert Fert and Peter Grünberg, Nobel Prize in physics 2007

have shown anisotropy in the spin dephasing time with respect to wire orientation. The origin of the signals is assumed to be from 2DEG and bulk spin ensembles. That brought us to a question whether the ballistic confinement of bulk spin ensemble can lead to anisotropy of the spin dephasing time like in 2DEG. The goal of this part of the project was to answer this question by doing numerical simulations.

The second part of the project is dedicated to the experimental measurements of the Kerr signal decay in moderately doped n-GaAs. These spin systems are already well studied and are known for their extremely long spin-dephasing times [11]. The effect we intended to study may well be present in other spin systems but our choice of n-GaAs was made due to the relative simplicity of this system with respect to other more complicated systems, such as heterostructure with quantum well.

In earlier studies on heterostructure we saw phase offset and g-factor drift that could not be explained. A typical Kerr signal from the sample put into magnetic field is shown on Figure 1 (black curve). Zero point on the time scale corresponds to the moment when spin polarization was excited in the system by pump pulse. This point should correspond to the first maximum of exponentially decaying cosine function. But when we try to fit experimental data with monotonically decaying cosine we should introduce additional phase offset in order to do better fitting, otherwise there is a big discrepancy between experimental data and fit in the tail of the curves (See Figure 1). There may be a several explanations for that. In this part of the project we would like to find out information about the evolution of the g-factor during the decay process and what effect it may produce on the phase offset. We would like to know when and why deviating g-factors and phase offsets are observed. Our goal is to experimentally investigate and establish what g-factor can occur, whether phase offset occur and systematically map out how these effects depend on experimental parameters.

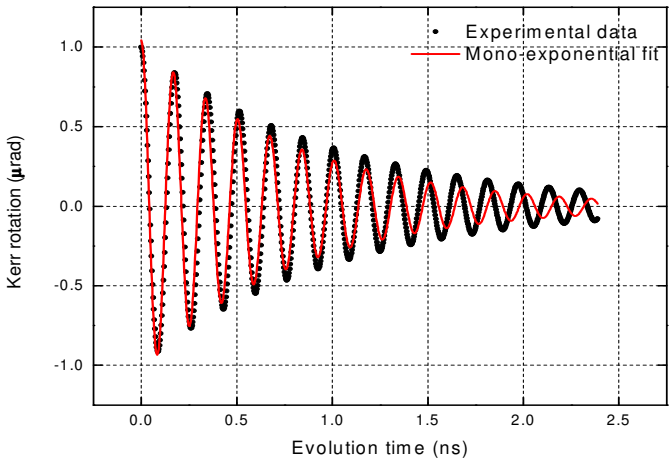

Figure 1 A typical Kerr signal from the sample inserted into magnetic field (~1 Tesla): experimental data (black curve), mono-exponential fit (red curve) with zero phase offset.

Outline of the thesis is as follows: in the second chapter of this thesis an introduction to the magneto-optical Kerr effect will be given. Also it will contain an overview on spin dephasing-mechanisms in general and particularly in semiconductors,

systems we are interested in. The description of the model used for the numerical simulations and the results of the simulations for confined bulk spin ensembles will be presented in chapter 3. Chapter 4 will provide description of the experimental Kerr setup and give the results of measurements.

This project is a master thesis which is a part of the second year of the Top Master Program in Nanoscience. This program is organized by Zernike Institute for Advanced Materials, University of Groningen. This work was done during the period from September 2008 till September 2009 in the group of Physics of Nanodevices.

2 Theory

2.1 Spin relaxation and spin dephasing

2.1.1. Introduction

Spin relaxation and spin dephasing are processes that lead to spin equilibration and are thus of great importance for spintronics. The easiest way to give definition of spin relaxation (T_1) and spin-dephasing (T_2) times is via Bloch equations, which describe time evolution of the average spin orientation $\langle \vec{S} \rangle$ of an ensemble in an applied magnetic field $\vec{B}$.

$$\frac{\partial \langle \vec{S} \rangle_x}{\partial t} = \gamma \left(\langle \vec{S} \rangle \times \vec{B} \right)_x - \frac{\langle \vec{S} \rangle_x}{T_2} \tag{2-1}$$

$$\frac{\partial \langle \vec{S} \rangle_y}{\partial t} = \gamma \left(\langle \vec{S} \rangle \times \vec{B} \right)_y - \frac{\langle \vec{S} \rangle_y}{T_2} \tag{2-2}$$

$$\frac{\partial \langle \vec{S} \rangle_z}{\partial t} = \gamma \left(\langle \vec{S} \rangle \times \vec{B} \right)_z - \frac{\langle \vec{S} \rangle_z - \langle \vec{S} \rangle_z^0}{T_1} \tag{2-3}$$

Where $\gamma = \mu_B g/\hbar$ is the electron gyromagnetic ratio.

Spin relaxation time T_1 (often called longitudinal or spin-lattice time) is the time that it takes for the longitudinal magnetization to reach equilibrium $\langle \vec{S} \rangle_z^0$ (to orient along the field). In this processes energy has to be taken from the spin system to the lattice, thus T_1 is responsible for energy relaxation processes.

Physical process that leads to the loss of the of transversal component of the spin originates from purely quantum mechanical property of the spin: quantum system that that is characterized by a quantum state entangles with the quantum state of the environment while interacting with it, thus loses its coherence. This process is irreversible and is called quantum decoherence or quantum dephasing. The characteristic time of the process is called decoherence time and is denoted T_2.

When we are dealing with the ensemble of spins another source of the loss of transversal component of the spins is present. A fluctuation of the magnetic field that may occur for example due to spin orbit interaction causes fluctuations of precession frequency. Unlike in quantum decoherence, these processes are reversible and can be eliminated by spin-echo experiment. This process is called inhomogeneous spin-dephasing. Often time parameter which describes spin-dephasing processes (quantum + inhomogeneous) is denoted T_2^* and $1/T_2^* = 1/T_2 + \gamma \Delta B$, where ΔB describes field fluctuation.

In simulation part (chapter 3) of this thesis we consider only inhomogeneous spin-dephasing, thus we assume $T_2 >> T_2^*$.

2.1.2. Mechanisms of spin relaxation

There are four mechanisms that cause spin-relaxation of conduction electrons in metals and semiconductors: the Elliot-Yafet, D'yakonov-Perrel', Bir-Aronov-Pickus and hyperfine interaction mechanisms. In the Elliot-Yafet mechanism electron spin relax because the electron wave function associated with a given spin have an admixture of the opposite spin states , due to spin orbit coupling induced by ions. The D'yakonov-Perrel' mechanism explains spin dephasing in solids without a center of symmetry. Spin-dephasing occurs because electrons feel an effective magnetic field , resulting from a lack of inversion symmetry and spin-orbit interaction, which changes in random direction every time electron momentum scattering takes place. More detailed description of this spin dephasing mechanism is given is sections 3.1 and 3.2. Bir-Aronov-Pickus mechanism is responsible for the spin relaxation in *p*-doped semiconductors , in which the electron hole exchange interaction gives rise to fluctuating magnetic fields flipping electron spin. Hyperfine-interaction mechanism is present in semiconductor heterostructures (quantum wells and quantum dots) based on semiconductors with nuclear magnetic moment. Spins of localized or confined electrons interact with nuclear magnetic moments, resulting in spin dephasing.

2.2 Magneto-optical Kerr effect

The magneto-optic Kerr effect was discovered by John Kerr in 1877 while he was examining the polarization of light reflected from a polished electromagnet pole. It consists is change of the polarization of the light being reflected from the magnetic (or magnetized) surface.

Macroscopic description of the magneto-optic Kerr effect is based on an analysis of the dielectric properties of a medium. In analogy with mechanical oscillations linearly polarized light may be expressed as a superposition of two circularly polarized modes. If the medium is not magnetized both of the modes are in the same condition and feel the propagation medium in the same way (dielectric constant and thus refraction index and velocity are the same). When magnetic field is applied it breaks time reversal symmetry of the system and propagation of the left and right circularly polarized light is no longer equivalent. There are two processes tacking place for light propagating in magnetized medium. First, the circularly polarized modes gain different phase shift due to their different propagation velocities, resulting in a rotation polarization plane. This process is the conventional Kerr rotation. Second, the different absorption rates of the medium for different polarization modes affect the ellipticity. In general, both effects exist in magnetized medium [3].

3 Simulation of the spin dephasing in 3D electron gas

3.1 Introduction

Spin-orbit interaction is a main source of the spin-dephasing in semiconductor materials with Zinc-Blend structure. In crystals without inversion symmetry it causes energy spin splitting of the conduction band [4]. Classically spin splitting of the conduction band is equivalent to electron moving in a certain effective magnetic field, magnitude and orientation of which are defined by the magnitude and the orientation of the electron wave vector. As the orientation of the electron wave vector differs for electrons in an ensemble of conduction band electrons, each electron feels different magnetic field. Precession of the electron spin ensemble in such effective magnetic field results in the spin dephasing that leads to the loss of the average spin orientation. Such mechanism of the spin-dephasing is called D'yakonov-Perrel (DP) spin-dephasing mechanism.

In view of a rapid development of the spintronics, it is important to be able to control spin dephasing. For that a number of studies, both theoretical and experimental, have already been done. Due to miniaturization trends in electronics low-dimensional systems appeared to be of particular interest. Recent numerical study [5] of the two-dimensional electronic gas (2DEG) within asymmetric quantum well has shown that spin dephasing time could be increased if 2DEG is ballistically confined to quasi-1D. Moreover, the spin-dephasing time strongly depends on the orientation of the ballistic confinement with respect to crystallographic axis. The reason for that lies in an anisotropic distribution of the effective spin-orbit field that has clearly distinguished low and high field directions. It was shown numerically [5] that the necessary condition for observing anisotropy is $L_{sp} > W$, where is L_{sp} the spin precession length, W is the width of the ballistic confinement. Experimentally such 2DEG systems were studied by time resolved Kerr rotation technique [6] and by time resolved Faraday rotation technique [7], and existence of the anisotropy for the spin dephasing was indeed proved.

One of the interesting results was presented in [6], where the spin relaxation of the 2DEG system, confined within the AlGaAs/GaAs quantum well, was studied. The observed Kerr signal originated from the two electron populations. It was shown that part of the signal comes from the electrons located in the quantum well. And another part was assumed to come from the bulk electrons from the substrate of the heterostructure. As it was anticipated, the signal from the 2DEG has shown anisotropy of the spin-dephasing. The spin-dephasing time for wire orientation along [110] crystallographic becomes longer with respect to the spin-dephasing time for wire orientation along [-110]. Interestingly, Kerr signal from the bulk electrons has also shown anisotropy of the spin dephasing time, which was not expected. The goal of the research presented in this chapter is to get more evidence that this signal indeed originated from the bulk electrons and to show that spin-dephasing anisotropy is possible also for bulk electrons. For that purpose 2D model developed in [5] was extended to 3D case and numerical simulations for spin-phasing process was carried out for 3D spin ensembles. Details of the model and the results of the simulations are given in sections 3.1 and 3.2.

3.2 Description of the model

3.2.1. Spin-orbit field distribution

As it was already mentioned, spin orbit fields cause spin-dephasing of the ensemble of spins. The total spin orbit field consists of two components: Dresselhaus field and Rashba field. The distribution of these fields is shown on Figure 2 [1].

Figure 2 (a) depicts Dresselhaus component of the field on the Fermi sphere. Dresselhaus field is a result of the inversion symmetry break in the crystal and in 2D case is dominated by a term linear in k; in 3D dominant term has a cubic dependence on k and is expressed by [1]:

$$\vec{B}_{Dresselhaus} = C_D(\vec{e}_x k_x(k_y^2 - k_z^2) + \vec{e}_y k_y(k_z^2 - k_x^2) + \vec{e}_z k_z(k_x^2 - k_y^2)) \quad (3\text{-}1)$$

where C_D is a Dresselhaus field constant and is defined by intrinsic properties of a particular crystal. k_x, k_y, k_z are the components of the electron's wave vector.

Rashba component appears in cases when electron feels electric field inside of a crystal. This electric field may occur as a result of the conduction band bending within a crystal (Figure 3), as it is the case in a p-n junction or in an asymmetric heterostructure. In 2D case asymmetric quantum well plays role of both a quantum confinement and a source of electric field. Confined electrons can move only in plane of the quantum well (Fig. 2). On the contrary, in 3D case electrons are not quantum confined within the quantum well and thus can freely move in all thee directions. But they still feel electric field, due to bending of the conduction band. That is why we also take into account Rashba field term in our model for 3D case as it was in 2D (electric field in z-direction) [1]:

$$\vec{B}_{Rashba} = C_R(\vec{e}_x k_y - \vec{e}_y k_x) \quad (3\text{-}2)$$

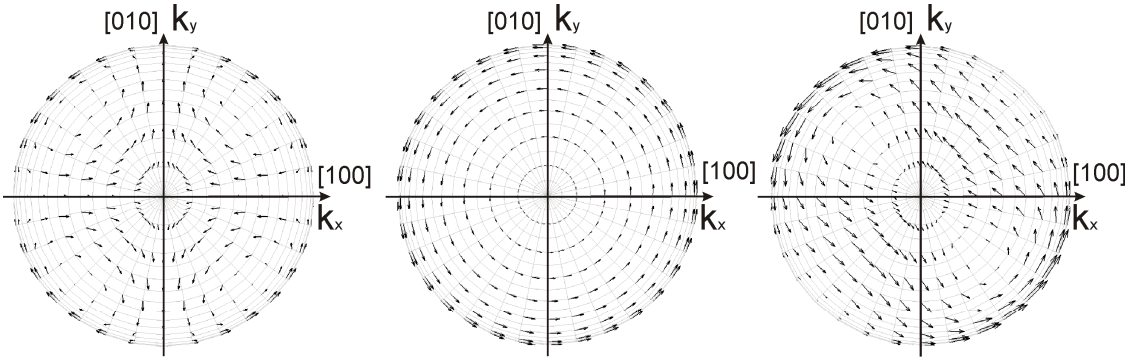

a) b) c)

Figure 2 Spin-orbit fields distribution over the Fermi sphere (projection on (001) plane) : (a) Dresselhaus field (b) Rashba field (c) Total effective field; [-110] – High field direction, [110] – low field direction

where C_R is a Rashba field constant. Distribution of the Rashba field on the Fermi sphere is depicted on Fig. 1 (b). In 2D case electrons move only in two directions. That is why they always feel the same electric field of the heterostructure, and therefore Rashba constant is independent of the electron's position. That is not the case in 3D, where electrons additionally freely move in the third direction (Fig. 3). Because the electric field of the heterostructure is not homogeneously distributed along the z axis (in our case [001]), Rashba constant is a function of the electron coordinates. We do not take this into

account in our simulations; instead we simplify the model and assume that Rashba constant is independent of the position of the electrons.

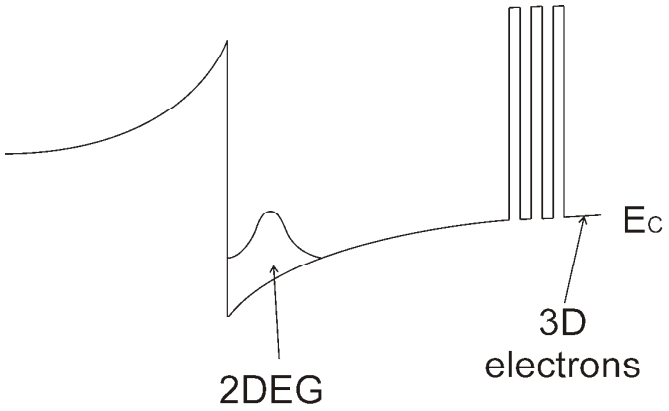

Figure 3 Bending of the conduction band in the crystal in the vicinity of the quantum well. Electrons in QW move only in two directions. 3D electrons propagate in all three directions and also feel bending of the conduction band.

Figure 2 (c) depicts a total spin-orbit field which is a vector sum of both Dresselhaus and Rashba components. It turns out that, as in 2D, it also can be highly anisotropic when Dresselhaus and Rashba fields are of the same order of magnitude. This chapter investigates whether spin-dephasing time in case of such spin-orbit field distribution would also show anisotropy.

3.2.2. Geometry of the system

In our model we consider ensemble of electrons that are classically moving inside of a 3D box (Figure 4). Each electron has a spin that is precessing in an effective magnetic field B_{eff}, which is a sum of external field and total spin-orbit field. Our goal is to find average spin orientation for the particular moment. For that, by applying Monte Carlo method, we keep track of the spin orientation of each individual electron and average spin over the ensemble for each particular moment. Each electron is assumed to move with Fermi velocity that is proportional to Fermi k-vector, which in its turn is defined by the free electron density n in the material:

$$k_F = (3\pi^2 n)^{1/3} \tag{3-3}$$

The whole evolution time is divided into small intervals, during which electron is moving and its spin is precessing around effective magnetic field (Fig. 4). The precession angle during small period of time Δt is expressed by the formula:

$$\varphi_{prec} = \frac{g\mu_B \left|\vec{B}_{eff}\right|}{\hbar} \Delta t \tag{3-4}$$

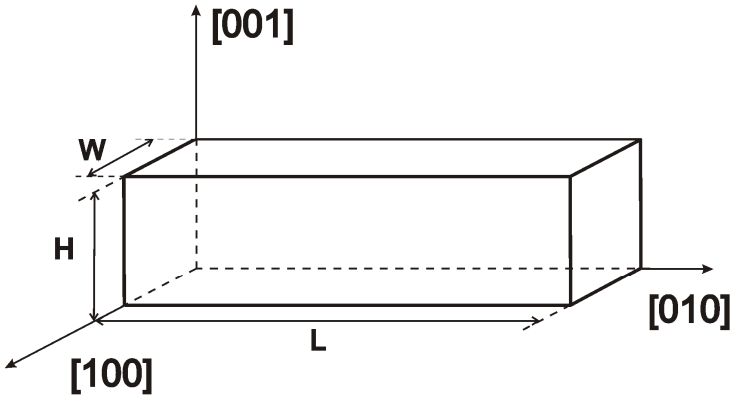

Figure 4 Single electron is classically moving within 3D box. The orientation of the box is shown with respect to crystallographic axis'.

The duration time of the interval Δt is chosen from the following consideration: 1) it should be smaller then the scattering time (scattering on the impurities) 2) The distance passed by electron during Δt should be smaller then the transverse size of a box (both W and H). If during that small time Δt electron scatters on the wall, then spin evolution is split into two stages: before and after scattering. During each of these stages electron feels different effective field.

Scattering on the impurities is also included in our model. Mobility is a main macroscopic parameter that characterizes scattering in the material (scattering time is proportional to mobility $\tau_{sc} = \mu m / e$). That is why we introduce scattering via mobility in our model. After each interval Δt electron is scattered with certain probability. This probability is defined by the relation between the scattering time and the duration of the interval $\sim \exp(-\tau_{sc} / \Delta t)$. If impurity scattering happens electron is scattered in random direction with equal probability for all directions.

The orientation of the electron spin is characterized by spin state at each moment of time. Suppose at the beginning electron had initial spin state $\left|\Psi_{initial}\right\rangle$. After precession in effective field electron evolved into the final spin state $\left|\Psi_{final}\right\rangle$ (Figure 5). Mathematically we can go from initial to final state by acting on the initial state with a time-evolution operator $\hat{U}:\left|\Psi_{final}\right\rangle=\hat{U}\left|\Psi_{initial}\right\rangle$.This operator is a function of the effective field and thus depends on the evolution interval we are considering:

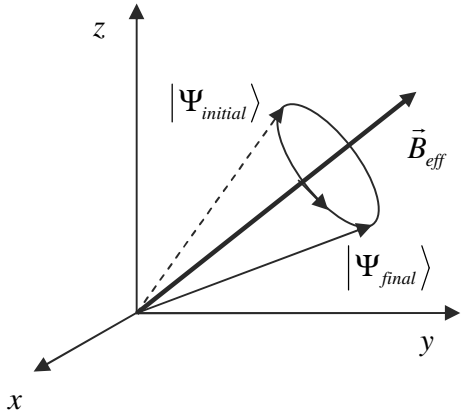

Figure 5 Spin of individual electron precess in effective magnetic field.

$$\hat{U}=\hat{U}(\Delta t_i)=\begin{pmatrix}\cos\frac{\varphi_{prec}}{2}-iu_z\sin\frac{\varphi_{prec}}{2} & -(iu_x+u_y)\sin\frac{\varphi_{prec}}{2}\\ -(iu_x-u_y)\sin\frac{\varphi_{prec}}{2} & \cos\frac{\varphi_{prec}}{2}+iu_z\sin\frac{\varphi_{prec}}{2}\end{pmatrix} \tag{3-5}$$

$\vec{u}=\vec{B}_{eff}/\left|\vec{B}_{eff}\right|$is a unit vector along effective magnetic field, Δt_i – i-th evolution interval. Thus at each evolution interval transition from initial to final state is accomplished by means of acting with time-evolution operator, for that particular interval, on the initial spin state, while the initial state is a final state from the previous interval. We are interested in temporal evolution of average spin orientation of the spin ensemble that can be expressed in form:

$$\left\langle S_r\right\rangle=\sqrt{\left\langle S_x\right\rangle^2+\left\langle S_y\right\rangle^2+\left\langle S_z\right\rangle^2} \tag{3-6}$$

where averaging in taken over the whole spin ensemble.

A number of parameters which describe our model and thus affect evolution of the spin ensemble can be varied. For example we can vary parameters that determine field distribution and its strength – Dresselhaus and Rashba constants. Free electron density also defines strength of the field. Because Dresselhaus and Rashba fields have third order and first order dependence on k-vector respectively, there exists a critical value of the electron density n_0 at which the magnitude of both fields is of the same order. That is why we can also vary Dresselhaus and Rashba constants by tuninng electron density around value of n_0, to change relative contribution of these fields into total spin-orbit field in our simulations. There are also parameters that define geometry of the system – width W and height H of the box (Figure 4). These parameters determine confinement of our system. And that is why by tuning them we are going to look how

confinement influences spin evolution; especially we are interested in the case when the size of the confinement is crossing spin-precession length. Possibility of adding external magnetic field is also included into our program.

To summarize, we are going to tune the following parameters of the system in course of our simulations:

1) The orientation of the confinement with respect to the crystal lattice.
2) Free electrons density around critical value n_0.
3) Width *W* and height *H* of the confinement (Figure 4).
4) Magnitude and the orientation of the external magnetic field.

All the numeric experiments were held for an ensemble of N=1000 spins. The value of the Dresselhaus constants was taken from work [8] where it was measured for the GaAs quantum well: $C_D = 10^{-24}$ T·m^3. The value of the Rashba constant was also measured in [8]: $C_R = 1.57 \cdot 10^{-8}$ T·m. As we do not consider here electrons being confined within quantum well but free electrons, we chose Rashba constant to be of the same order but smaller then the one obtained in [8]. For the rest of the calculations we used $C_R = 3.57 \cdot 10^{-9}$ T·m value of the Rashba constant. The density of the free electrons was chosen from the considerations of being realistic and being close to the value n_0 when Dresselhaus and Rashba fields become of the same order of magnitude:

$$n_0 = \frac{1}{2\pi^2}\left(2\frac{C_R}{C_D}\right)^{3/2} \tag{3-7}$$

For the chosen values of Dresselhaus and Rashba constants $n_0 = 3.06 \cdot 10^{22}$ m^{-3}. These parameters of the system are fixed for all simulations (Where needed additional explanations are given.). Initially all the spins are oriented along z-axis (incidence laser beam axis).

3.3 Results of the simulations

3.3.1. Temporal evolution of the average spin of an ensemble

In this section we present our first results of the simulations. Because we expected to see different spin dephasing times for different orientation of the confinement, for the beginning we ran our simulation for ballistic confinement orientated along high and low spin-orbit field directions, namely along [-110] and [110] directions. The results are presented on Figure 6. We can see different traces of average spin evolution for each direction. Spin-dephasing time T_2^* is determined as a time at which average spin decays *e* times comparing to the initial value. For the traces shown on Figure 6, T_2^* equals 367 ps and 124 ps for [110] and [-110] wire orientations respectively.

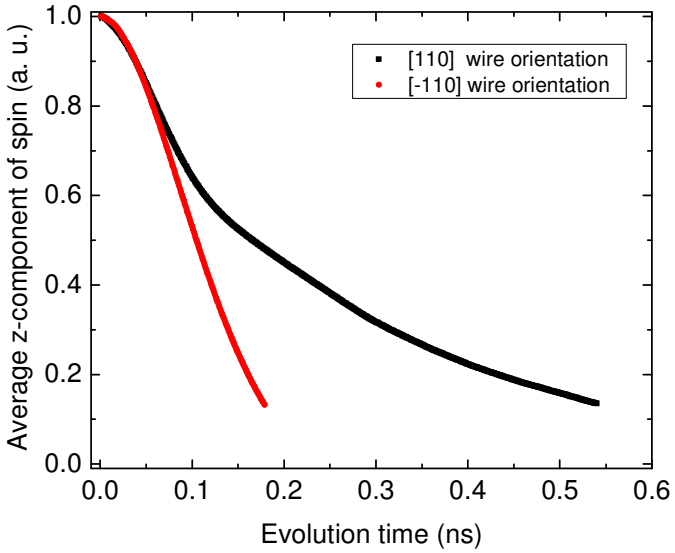

Figure 6 Typical trace of the time evolution for the average z component of spin for the spin ensemble.

3.3.2. Spin-dephasing time for different wire orientation

After proving that anisotropy of the spin dephasing indeed exists, we are going to investigate how it is affected by changing relative contribution of the spin-orbit fields. As it was already mentioned the magnitude of the spin orbit fields is defined by the Fermi k-vector of the electron, which in its turn depends on the concentration of the free electrons. At $n = n_0$ value of the electron density spin orbit field along [110] orientation equals zero (Figure 2), because Dresselhaus and Rashba components exactly cancel each other. And this is the reason for observing anisotropy of the spin-dephasing time. By detuning electron density from the critical value n_0 we change relative contribution of the Dresselhaus and Rashba terms to the total spin-orbit field and thus the field along [110] direction is no longer zero. That would lead to the disappearance of the anisotropy.

To chose a reasonable scattering parameter, that is electron mobility in our case, first a set of simulation processes was performed for different electron mobilities. Figure **7** show dependence of the spin-dephasing time T_2^* on wire orientation for different mobilities. We can see that [110] wire orientation corresponds to maximum spin dephasing time and [-110] corresponds to minimum spin-dephasing time for all mobilities. That is why we can introduce anisotropy parameter that is ratio between spin-dephasing times wire orientations along [110] and [-110] crystallographic axis's: $a = T_2^*[110]/T_2^*[-110]$. Obviously, anisotropy parameter decreases as the mobility becomes lower. That is understood because with then scattering on the impurities starts to play dominant rolore rather then scattering on the confinement. As we want to study anisotropy, for further simulations we fix mobility at the value $\mu = 300$ m^2/V·s. Figure 8 depicts spin-dephasing time T_2^* as a function of wire orientation for different values of the electron density. Dependence of the anisotropy parameter is shown on Figure 9. As we can see, maximum anisotropy is observed at $n = n_0$ value of electron density.

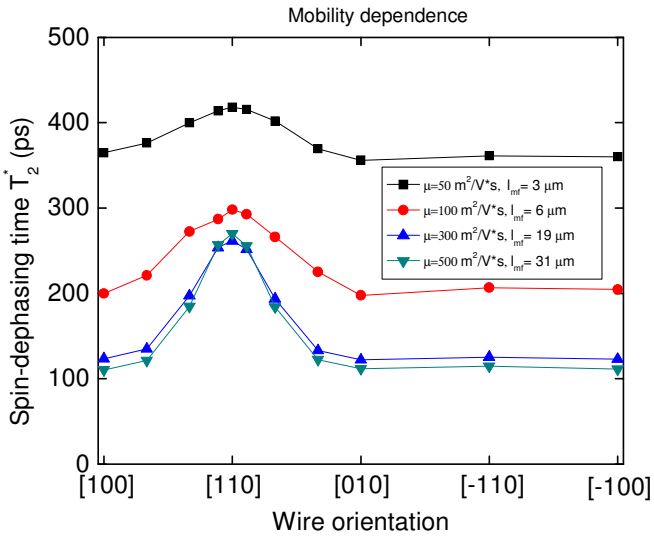

Figure 7 Spin-dephasing time dependence on wire orientation for different electron motilities. $n = n_0$

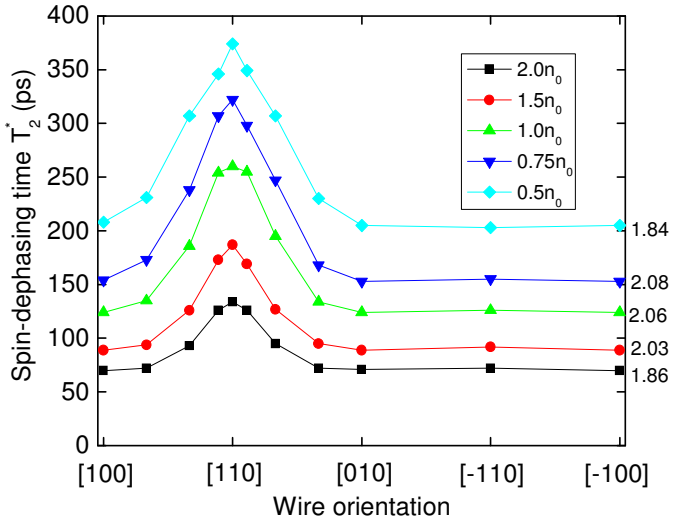

Figure 8 Spin-dephasing time for different free electron densities and wire orientations. Calculated anisotropy parameters for different electron density are put next to corresponding curves.

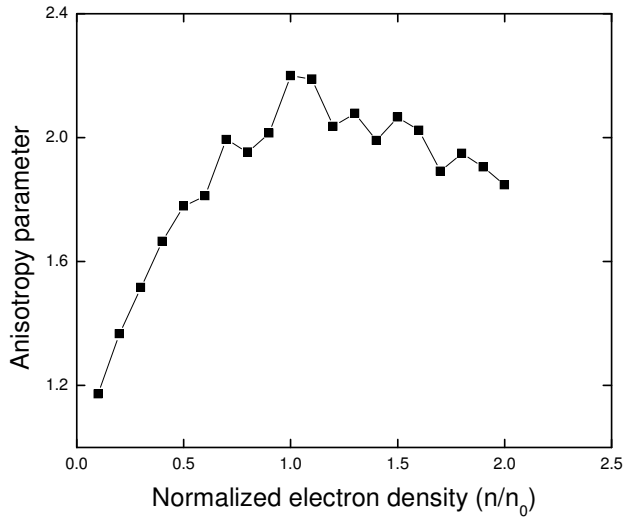

Figure 9 Anisotropy parameter $a = T_2^*[110]/T_2^*[-110]$ of the spin-dephasing time for different electron densities.

3.3.3. Spin-dephasing for different wire width and height

Confinement is a main reason for observing anisotropy of the spin-dephasing time. That is why we would like to know how will change of the width and height (the main parameters of the confinement) of the wires influence it.

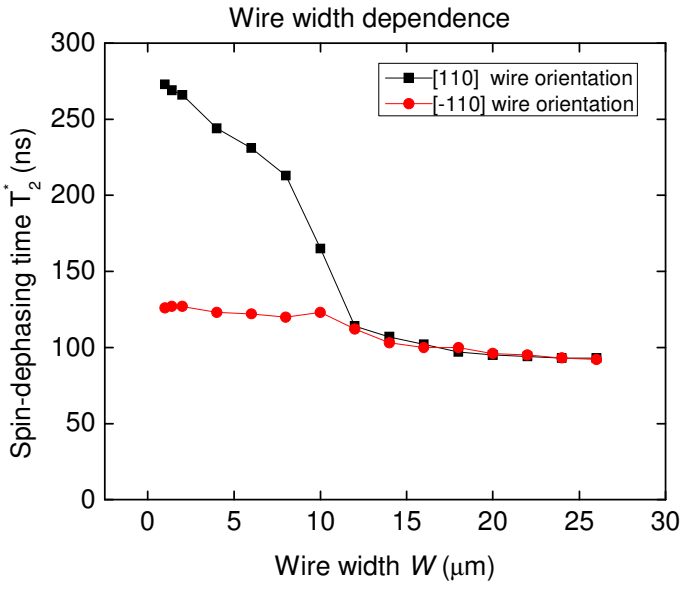

Figure 10 Dependence of the spin-dephasing time T_2^* on the wire width W. Other parameters fixed: $B_{ext} = 0$; wire height $H = 1$ μm; $n = n_{0.}$

Figure 10 shows dependence of the spin dephasing time on the width of the wire for [110] and [-110] wire orientations. As we can see at a certain value of the wire width

($W \sim 14\ \mu m$) T_2^* for [110] wire orientation rapidly drops down. If we calculate now spin precession length (that is the length passed by electron while its spin makes one half full circle of precession) along high field direction we obtain $L_{sp} \sim 17$ µm. That is why we may conclude that as long as the width of the confinement is smaller then the spin precession length electron ensemble feels it and we observe anisotropy of spin-dephasing, otherwise electron ensemble behaves as it was unconfined.

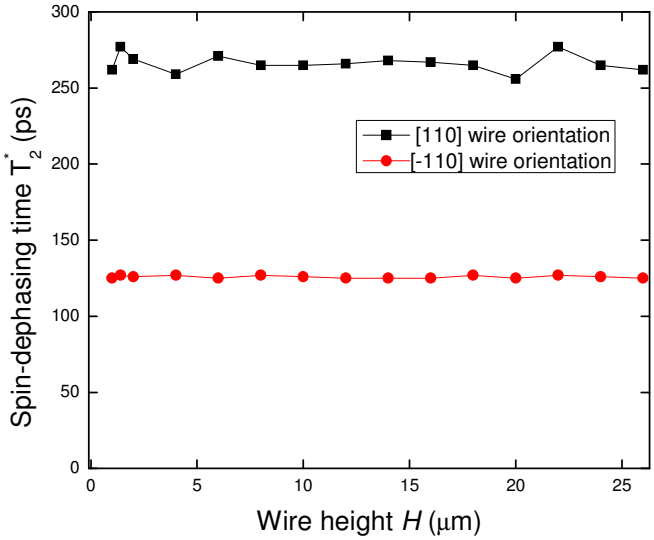

Figure 11 Dependence of the spin-dephasing time T_2^* on the wire height H. Other parameters fixed at: $B_{ext} = 0$; wire width $W = 1.4$ µm; $n = n_0$.

We also varied height H of the wires. The results are presented on Figure 11. For the first sight it is quite strange result comparing to the previous one. Spin dephasing time seems to show almost no dependence on the confinement size along [001] direction. But if we make a closer look at field distribution everything becomes clear. If we look at formulae (1) and (2) we can see that both Dresselhaus and Rashba components are zero for [001] direction of k-vector and fields in the vicinity of [001] direction is much smaller then fields in [110] direction. That means that movement of the electrons in the vicinity of the [001] is not a dominant source of spin-dephasing. That is why confinement in that direction does not strongly influence spin dephasing.

3.3.4. Influence of the external magnetic field on the spin-dephasing time

In previous section we have shown that wire width being smaller then spin-precession length ($W < l_{sp}$) is a necessary condition of observing anisotropy of the spin-dephasing. We showed it by changing relation between wire width and spin-precession length, while keeping the latter constant. The interesting question arises: what will happen if we keep wire width constant and very spin precession length? In other words, is it possible to control spin dephasing by controlling spin-precession length? To answer this question we included external magnetic field into our simulation.

First we studied how magnetic field influences spin-dephasing in a system without ballistic confinement ($L \to \infty$). The results of the simulations for two orthogonal field orientations are presented on Figure 12. At zero magnetic field T_2^* is identical for two orientations, as can be expected due to the symmetry. As the magnetic field increases spin-dephasing time for both field orientations also increases and saturates at certain field magnitude (~ 2 T), but the saturation values of T_2^* are different. Saturation occurs at external magnetic fields comparable with spin-ornit fields. This field anisotropy of the spin-dephasing may be explained from geometrical considerations: fields applied in different directions force electrons precess in different plains (the higher the field the more orientation of the plain if defined by the external field and not spin-orbit field). Thus spins that precess in different plains feel spin-orbit field in different way (since it is highly anisotropic, see Figure 2 (c)). This results in different spin-dephasing times for different external magnetic field orientation and is in agreement with the experiment [10].

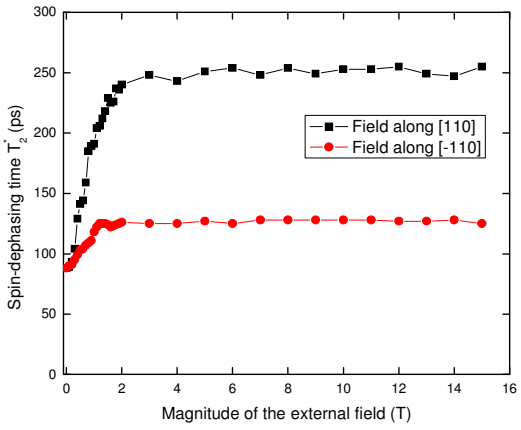

Figure 12 Dependence of the spin dephasing time T_2^* on the magnetic field in the system without ballistic confinement (without wires). Two orthogonal orientations of the field are considered

Further dependence of the spin-dephasing on external magnetic field was studied for the balistically confined spin ensembles. Simulations were carried out for two orthogonal orientations of the field (along [110] and [-110] crystallographic directions) and different orientations of the field. The results are presented on Figure 13. As we can see from Figure 13 (a), for the case of field and wires being perpendicular to each other , spin dephasing time does not depend strongly on the magnitude of magnetic field and is mainly defined by the orientation of the wires. On the contrary, in case of parallel wire and field orientation, spin-dephasing time increases with magnetic field for both [110] and [-110] wire orientation. It can be explained by the fact that, in this case, spin dephasing is strongly suppressed by confinement when spin rotated (n+1/2)π from initial position and becomes parallel to xy plane. To confirm this, additional simulation checks without magnetic field and with spin being initialized in xy plane were made.

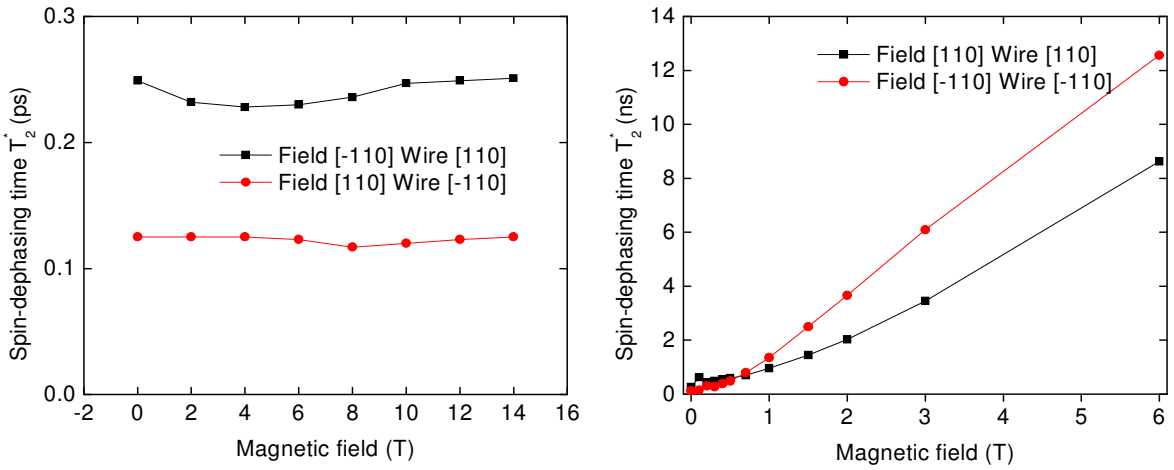

a) *b)*

Figure 13 Dependence of the spin dephasing time T_2^* on the magnetic field in the system ballistic confinement (with wires). Two orthogonal orientations of the field are considered: field and wire orientations are perpendicular to each other (a) and field and wire orientations are parallel to each other.

4 Spin-dephasing in n-GaAs

4.1 Introduction

A realization of the importance of GaAs systems for spintronics and quantum computing came after discovery of rather long spin-relaxation times (more than 100 ns) in *n*-doped GaAs samples.

Optical orientation and time-resolved spectroscopy methods were used to study spin relaxation in *n*-GaAs. In the earliest studies of the spin orientation dynamics in *n*-$Al_{0.3}Ga_{0.7}As$ with concentration of donors $N_d \sim 1\times10^{16}$ cm^{-3} at 4.2 K is was found spin relaxation time was found to be $\tau = 1.2$ ns [13]. A much larger spin life time was found by optical orientation on *n*-GaAs [14], where for $N_d \sim 1\times10^{15}$ the observed $\tau = 42$ ns. Faraday rotation studies performed Kikkawa and Awschalom on a series of *n*-GaAs samples with different concentration of donors have showed even longer spin life times [11].

Spin-relaxation time in *n*-GaAs as a function of donor concentration is shown on Figure 14. This is non monotonic dependence with a maximum around $N_d \sim 3\times10^{15}$. Three distinct regions may be specified in this dependence, each of which is a result of corresponding spin relaxation mechanism that dominates. The maximum at $N_d \sim 3\times10^{15}$ is due to the crossover between relaxation mechanisms originating from the hyperfine interaction with lattice nuclei and from the spin-orbit interaction [12]. The peculiarity at $N_d \sim 2\times10^{16}$ is associated with the metal-insulator transition [11]. It reflects the change of the specific mechanism through which the spin-orbit coupling affects the spin lifetime: in the metallic phase it is the D'yakonov-Perrel mechanism, while in the insulator phase ($N_d < 2\times10^{16}$) it is the anisotropic exchange.

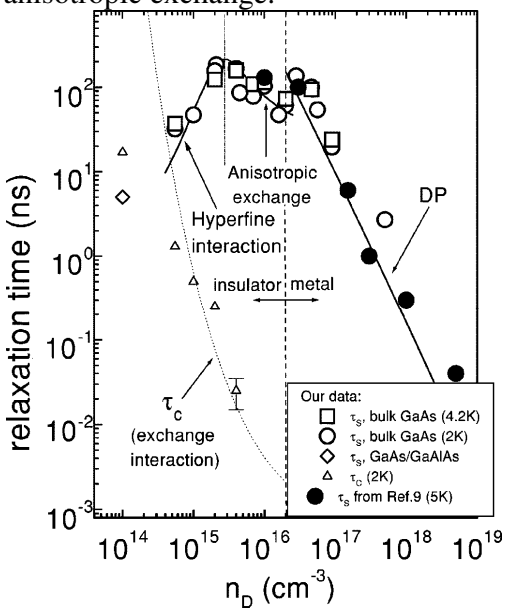

Figure 14 Spin-relaxation time as a function of donor concentration in *n*-GaAs. Solid line: theory. Figure taken from [12].

In this chapter we present the results of hte time resolved Kerr rotation measurements on the *n*-GaAs sample with concentration of donors $N_d \sim 2\times10^{16}$. The

detailed description of the sample is given in the following section. The description of the setup and the results are given in sections 4.3 and 4.4 corrispondingly.

4.2 Description of the sample and band structure

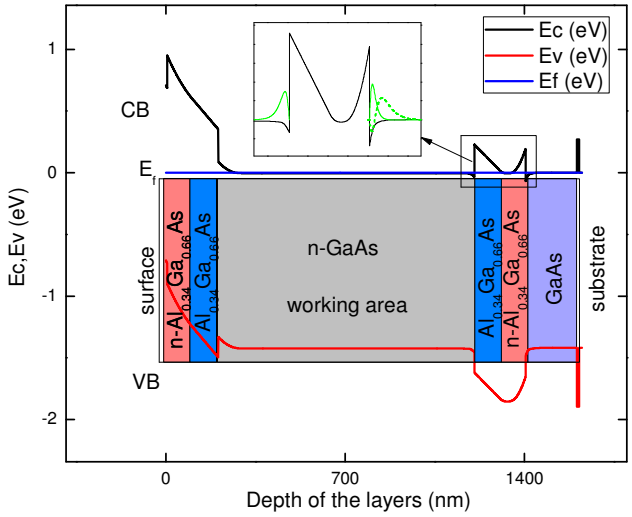

Figure 15 Band diagram and sample structure. The inset shows possible quantized stated in heterostructure (Green curves are wave functions of these states).

Measurements were performed on GaAs sample grown by molecular beam pitaxy in group of A. Wieck from Ruhr University in Bochum [16]. The sample was grown on GaAs substrate and it's structure consists of 9 layers (See Table 4-1). The active layer has an electron density of $n = 2\times10^{16}$ cm^{-3} and mobility $\mu = 5200$ cm^2/V·s at room temperature. The active area is sandwiched by undoped spacer and doped $Al_{0.34}Ga_{0.66}As$ to prevent surface recombination and unwanted spin diffusion into the substrate and

Layer	Doping, cm^{-3}	Thickness, nm
GaAs		5.0
$Al_{0.34}Ga_{0.66}As$:Si	7×10^{16}	100.0
$Al_{0.34}Ga_{0.66}As$		100.0
GaAs:Si	2×10^{16}	1000.0
$Al_{0.34}Ga_{0.66}As$		100.0
$Al_{0.34}Ga_{0.66}As$:Si	1.5×10^{16}	100.0
GaAs		200.0
AlAs		10.0
GaAs		10.0

Table 4-1 Growth data of the n-GaAs sample

surface. The doping levels of these layers were chosen to be 7×10^{16} cm^{-3} and 1.5×10^{16} cm^{-3} above and below the active layer, respectively, to flat band for n-GaAs layer. The AlAs layer near the substrate was grown as a potential etch-stop, so that the heterostructure may be removed from the substrate if needed.

Band structure of the sample is calculated by solving Poisson equation with boundary conditions. That was done by using program which solves 1D Poisson equation [14]. This program uses standard finite difference method to solve linear differential equations with given boundary conditions. Another good point in this program is the possibility of solving one-dimensional Schrödinger equation for a given potential. It uses solution of the Poison equation as an input potential profile for Schrödinger equation and gives as a result wave functions of the quantized states. The results of the calculation are presented on Figure 15. As we can see the conduction and valence bands are almost flat in the working area. That proves that doping and thicknesses of the spacer layers were chosen correctly. Band banding on both sides of the bottom spacer layer seems to be potential source of quantized states of the electron gas. The solutions of the Schrödinger equation are presented on the inset of the Figure 15. As we can see there are two quantum wells (QW), one of which has only one quantized state and another one two states, are located around 1 μm under the surface. The corresponding energies are E-E_f=7.09×10 eV for upper QW and -14.3×10^{-3} eV and -1×10^{-3} eV for the lower QW.

The drawback of presented band structure simulations is that Poisson and Schrödinger equations are not solved self consistently. First Poisson equation is solved for a given boundary conditions and then Schrödinger equation is solved using the results from Poisson equation. Although Poisson solution gives quite good first order estimation of the band structure, self consistent solution of the system of Poisson and Schrödinger equation is required for calculation of the quantized states that could be present in heterostructure.

4.3 Experimental setup

One of the techniques that is used to investigate spin dephasing and relaxation in metals and semiconductors is time resolved Kerr rotation technique (TRKR). This is a pump-probe technique which utilizes circularly polarized pump pulse and linearly polarized probe pulse that are delayed in time with respect to each other. Circularly polarized pump directed toward a particular spot on the surface locally generates nonequilibrium spin polarization. By sending linearly polarized probe pulse into the same spot and by observing change in polarization of the reflected beam one can trace time evolution of the average spin orientation.

Figure 16 schematically shows the most important components of the system. One can distinguish three main stages of the experimental process while running measurements: 1) generation of the needed pump and probe pulses that includes their delay in time, modulation and filtering 2) focusing of the beams on the same spot of the sample 3) detection of the reflected probe and measurements of its polarization state change. The instruments that realize first stage are shown on (a) part of the scheme and the last two stages are implemented with instruments on part (b). A detailed description is given in the following subsections.

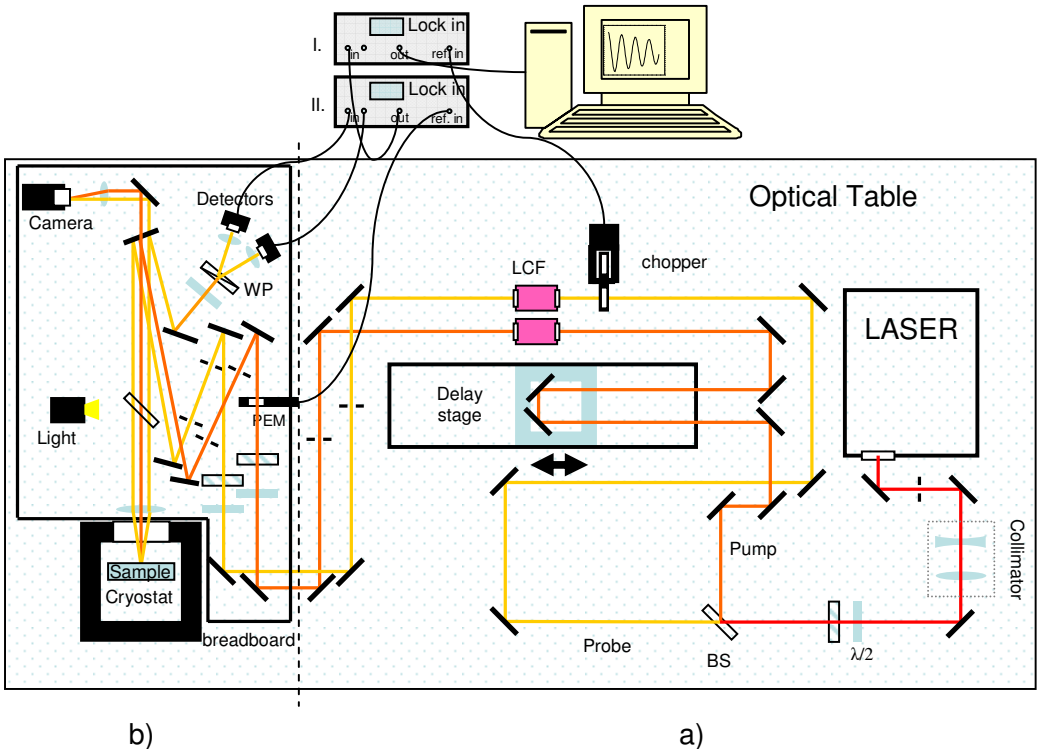

Figure 16 Scheme of the experimental setup. (a) Splitting of the initial beam into pump and probe, their separation in time, modulation and filtering is realized in this part of the setup (b) Positioning of the beams on the sample, imaging and detection system are located on the breadboard. Pump and probe are marked with orange and yellow colours accordingly; P - polarizer, λ/2-plate, BS – beam splitter, LCF – liquid crystal filters, WP – Wollaston prism, PEM – photo-elastic modulator. For detailed explanation of all the elements see main text.

4.3.1. Pump-Probe Delay, Modulation and Filtering

In this section we are going to describe the part of the optical setup which give as an output two pulsed beams, one of which is circularly polarized pump and another one linearly polarized probe. The later is delayed in time, modulated and filtered (Figure 16 a).

The first and the most important element of this part of the setup is a pulsed Ti:Sapphire laser. This is an ultrafast laser that works in pulsed regime with a repetition rate 80 MHz (12 ns distance between pulses, pulse duration 150 fs). This allows us to study physical processes that last less then 10 ns. In cases of longer lifetimes resonant amplification effects may occur that is pumping of the system that is not fully relaxed [11]. To avoid this pulse peaker may be used. The wave length of the laser is tunable within the range 690-1040 nm (it corresponds to photon energies 1.19-1.80 eV) with a spectral width around 8 nm.

As the laser beam gets out of the laser it is collimated by the pair of lenses. Due to the fact that we always deal with non-ideal Gaussian beams it is not possible to get perfectly collimated beam. This is important for the pump beam which goes through the delay line and for different positions of the delay line it passes different distances to the surface of the sample. This results in the drift of the diameter of the beam when the delay line is moving and thus results in the change of photon density. To minimizes this undesirable effect beam is collimated in such a way that the neck of non ideal Gaussian beam is put in the middle of the delay line. The diaphragm that is put before the collimator is purposed to prohibit back reflection of the beam. After collimator the laser beam goes thought λ/2-plate and polarizer. This pair of elements allows to control intensity of the outcome beam. Polarizer sets initial light polarization for the whole system (that is why it is always fixed) and λ/2-plate controls polarization of the beam before entering polarizer. Although λ/2-plate works properly only for a particular wavelength it is enough to work as a controller of beam intensity. This could be done by another polarizer but polarizers, bases on the Glan prim, strongly deflects beam comparing to plate.

Further beam is splitted into pump and probe by the beam splitter. 80 % of the pulse energy goes to pump and 20 % goes to probe. Further pump pulse is sent to the computer controlled delay stage which allows to set time delay between pump and probe pulses. It is very important and precise element of the system and should be properly aligned before other elements that follow it. The position of the delay line is controlled with a precision 0.1 μm and it allows us to delay pump and probe pulses with a precision of 0.33 fs with respect to each other.

To create nonequilibrium spin polarization we need circularly polarized light. That is why pump pulse after being delayed is sent through the photo-elastic modulator (PEM) (Figure 16 (b)). PEM is a device which modulates initially linearly polarized light between left and right circularly polarized light at a frequency 50 kHz. We use PEM instead of normal λ/4-plate because we want to avoid dynamic nuclear spin polarization in the sample so that on a long time scale the average spin injection is zero [22].

After beam splitter probe pulse is modulated with chopper at a frequency 169 Hz. This is done to separate Kerr signal from the signal that is coming from diffusively scattered pump. Because in our setup both pump and probe are modulated this is called double modulation technique. If we prevent scattered pump from entering detectors (that could be done by filtering in case of double colour experiment) chopping of the probe

beam would not be necessary and we would use single modulation technique which can be much faster.

As we want to study photon energy dependence of relaxation processes in n-GaAs we would like to have better resolution over the frequency that can not be achieved simply by tuning laser (spectral width ~ 10 nm). For that we use liquid crystal filters which can be easily tuned by applying voltage and give spectral line width of the order 2-3 meV (For more detail see Appendix A).

4.3.2. Focusing, Imaging and Detection

As the pump and probe pulses are delayed with respect to each other, modulated and filtered they are ready to be positioned upon the surface of the sample. In order to control the positioning of the pump and probe beams imaging and steering optics is used. All the elements are installed on the breadboard (Figure 16 (b)). With the steering mirrors pump and probe are directed parallel to each other to the entrance mirror of the cryostat. Convex lens (focal length 17 cm), in front of the window of the cryostat, focuses pump and probe at a single spot on the surface of the sample. Pump enters the surface at zero incidence angle and probe is tilted (~1°). After reflection from the surface of the sample both beams leave the cryostat and further are splitted by the beam splitter. Part of the beams that goes through the beam splitter is further directed and focused on the CCD camera. Pump reflected from the beam splitter is lost and probe is steered to the detection system.

To be able to control positioning of the laser beams on the sample, the surface of the sample should be visible. For that purpose sample can be illuminated by white light from the diode (during Kerr experiment it is turned off). The focusing and imaging is done with the same optics as for the laser beams. Thus the focusing/imaging system allows us to have images of both the surface of the sample and of the laser beams on the display of the computer. By tuning the actuator of the lens holder we can control position of the beams point of incidence on the sample surface. Knowing the focal length of the lens and the displacement of the lens holder actuator we can measure diameter of the beam spot on the surface. In our case the diameter of the probe at the surface of the sample was 50-100 μm. In order to measure diameter of the beam with higher accuracy one can use knife-edge technique .

The detection system consists of a balanced polarization bridge, which is a pair of photodiodes, and measures change of the polarization of the reflected probe beam. The probe reflected from the surface of the sample is steered to the Wollaston prism (WP) which splits it into two beams: with s- and p-polarization accordingly. Each of these two beams is further focused on the corresponding photodiode. Kerr signal is proportional to the difference of the intensities of s- and p-polarized beams. Before running the experiment polarization bridge is being balanced. That means that when spin polarization imbalance in the sample is zero the signal from the bridge is also set to zero. This is achieved by adjusting the polarization of the probe beam (using λ/2-plate before the Wollaston prism) in such a way that intensities of s- and p-polarized beams after Wollaston prism are exactly equal to each other, while pump beam is blocked. By unblocking pump spin polarization imbalance is introduced into the system, that results in change of the probe polarization and thus breaks balance of the diode bridge. The signal from the bridge becomes non-zero and this is the useful (Kerr) signal we want to measure.

As the balancing of the diode bridge is complete pump is unblocked and optimal overlap of the pump and probe is being adjusted (by tuning mirrors that steer pump). At the output of the diode bridge we have Kerr signal that is double-modulated: 1) PEM modulation 2) chopper modulation. In order to retrieve Kerr signal two lock-in amplifiers are used. The signal from the diode bridge is sent to the lock-in I (Figure 16)). This lock-in is synchronized with PEM and gives single-modulated Kerr signal at the output. Further this signal is sent to the second lock-in which uses reference signal from chopper. At the output of the second lock-in amplifier finally Kerr signal is measured.

4.3.3. Temperature Control and Sample Positioning System

A magneto-optical cryostat is used to control sample temperature and to apply magnetic field (Figure 17 (a)). The sample is cooled down by helium gas that that is coming from liquid helium chamber. It allows to set and keep constant temperature of the sample in a range of 2.2-300 K. Split pair magnet allows to provide magnetic field up to 7 Tesla. It is located in the bottom part of the cryostat in such a way that it creates horizontal magnetic field in the sample space. The whole system is installed on the optical table next to the convex lens on the breadboard, so that the sample could be reached by laser beams via window of the cryostat.

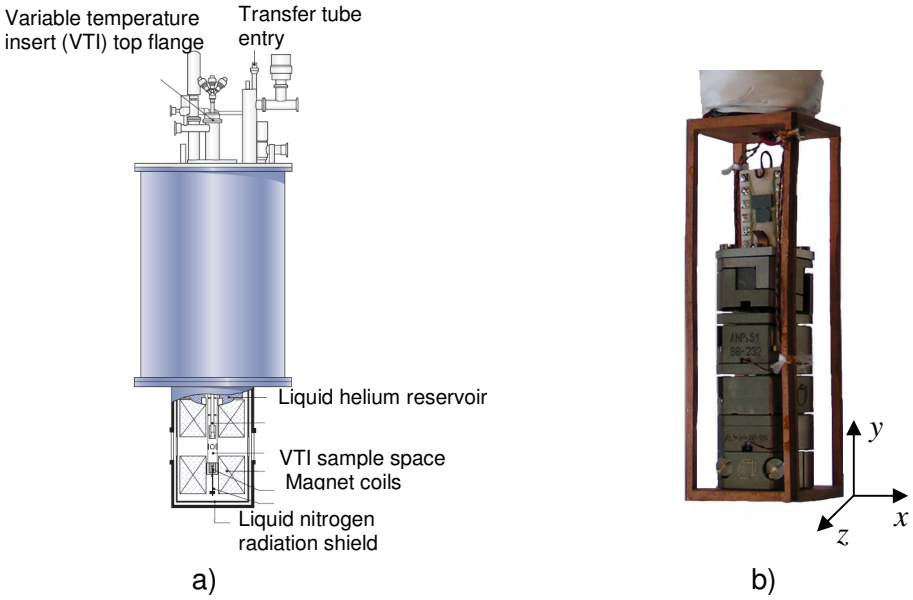

Figure 17 Schematics of the Cryostat (a); Sample positioning system in a copper holder (b)

The sample is located is the bottom part of the cryostat on a sample holder which is connected to the end of the variable temperature insert (VTI). We measure TRKR in Voigt geometry: magnetic field is parallel to sample plane, laser beams are perpendicular to sample plane. The sample holder is made of copper and it is shaped as a box (Figure 17 (b)). The holder serves as a housing for four stage attocube system with a sample on the top of it. With the piezo crystal forming the basis of its functioning, attocube piezo-motor system allows positioning the sample in four dimensions with high accuracy. Three of

the stages provide positioning of the sample in XYZ directions with a sub-nm resolution in fine positioning mode. Travelling range is approximately 3 mm that allows measuring several devices on a single sample. The forth stage allows rotation of the sample in XY plane with a typical minimum step size 0.02 mº (at 4.2 K). All the elements of the holder and attocube system are made of non-magnetic materials to minimize distortion of the magnetic field from the coils.

4.4 Results and Discussion

In this section we present results of the experimental measurements. As it was explained in the introduction, we want to get deeper insight into the dynamics of the spin-dephasing of the bulk n-GaAs spin ensembles. Namely we are interested in the origin of initial phase shift of Kerr signal, possible drift of the g-factor, and possible interconnection between these two phenomena. For that we have performed TRKR study of n-GaAs sample for different parameters of the system. We varied such parameters of the system as pump power, pump/probe wavelength, pump/probe spectral linewidth, magnitude of the external magnetic field (which is applied in plane perpendicular to laser beam and in plane of the sample).

A typical Kerr signal, which is a time dependence of Kerr rotation, is show on Figure 18. When external magnetic field is applied to the system, Kerr signal approximately is an exponentially decaying cosine function. For two different magnetic fields it oscillates with different frequency that is proportional to magnetic field.

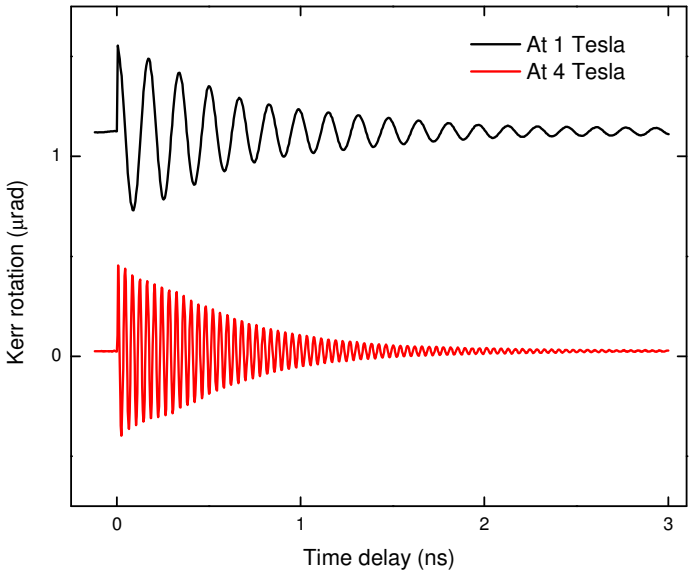

Figure 18 Typical oscillations of Kerr signal when external magnetic field is applied to the system. Pump power is 10 mW. λ_{pump} = 814.5 nm, λ_{probe} = 819 nm

In order to retrieve useful information from experimental data, such as spin-dephasing time and g-factor one needs to perform fitting of these data with model functions. The most trivial model function is mono-exponentially decaying cosine:

$$\theta_k(t) = A \cdot \exp\left(-t/T_2^*\right) \cdot \cos\left(g \frac{\mu_B}{\hbar} Bt + \varphi \right) \quad (4\text{-}1)$$

A typical fit of the experimental data with (4-1) is shown on Figure 19 (red curve). For this fitting phase φ in (4-1) was considered to be a free parameter. As we can see from the inset there is quite a big phase mismatch between experimental data and fit in the tale section of the Kerr signal. Since (4-1) fit initial part of the Kerr signal reasonably good, there might be g-factor drift present in the experimental data. Thus to improve fitting we must modify our model function. We do this by introducing time-dependent g-factor function $g(t)$in stead of constant g-factor g in (4-1):

$$\theta_k(t) = A \cdot \exp\left(-t/T_2^*\right) \cdot \cos\left(g(t) \frac{\mu_B}{\hbar} Bt + \varphi \right) \quad (4\text{-}2)$$

$$g(t) = g_2 + (g_1 - g_2) \cdot \exp(t/\tau_g) \quad (4\text{-}3)$$

Thus we assume that, at the time, we are observing Kerr signal, g-factor is exponentially decaying from initial value g_1 to final value g_2. A characteristic time of this evolution is τ_g A, T_2^*, φ, g_1, g_2, τ_g are the parameters of the fit. To get first good estimates of initial and final g-factors we first make a fitting of first 300 ps and last 1 ns of the data trace with (4-1) model function. Once we obtained g_1 and g_2 we perform fitting with fitting function (4-2) and use them as initial fit parameters. A typical fit of the of the Kerr signal with a function that takes g-factor drift into account is shown on Figure 19 (green curve). Comparing to mono-exponential fit it gives better results.

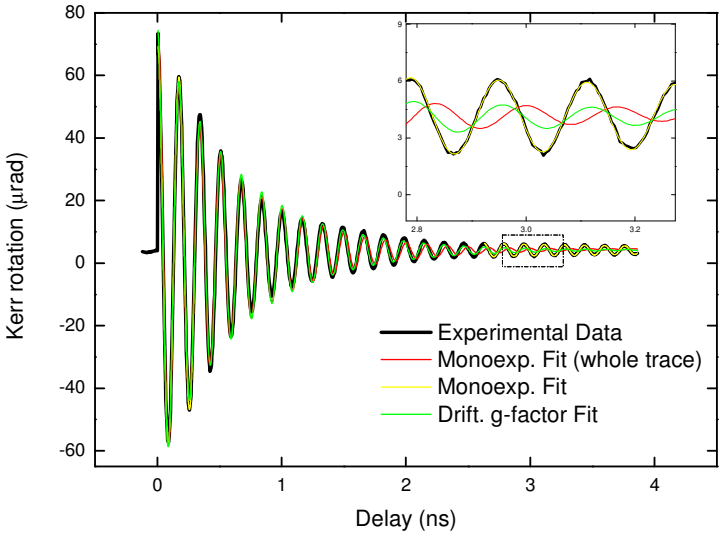

Figure 19 Fitting of the experimental curves: Black curve – experimental data; Red – mono-exponential fit within the whole time range of the trace (~ 4ns); yellow – mono-exponential fit of the first 300 ps and last 1 ns of the trace; Green – mono-exponential fit with drifting g-factor. Pump power is 15 mW. λ_{pump} = 814.5 nm, λ_{probe} = 819 nm

In course of our research we were interested in pump power dependence of the g-factor. For this purpose, a series of experimental Kerr signal curves was taken for power

of pump pulses in a range from 0.05 mW to 25 mW. The rest of the parameters were fixed. Both pump and probe pulses had narrow linewidth (~ 1-1.5 nm) since both were filtered by LCF. After fitting g-factor dependence on pump power was obtained (Figure 20). We can see a gradual increase of the absolute value of the g-factor as the pump power decreases from 0.41 to 0.445 where it reaches a kind of a plateau. By further decrease of the pump power g-factor increases even more rapidly and reaches a value of 0.483 at the experimental limit of pump power. This result is quite unexpected since in a number of papers reported value of g-factor in GaAs was –0.44 [11], [17].

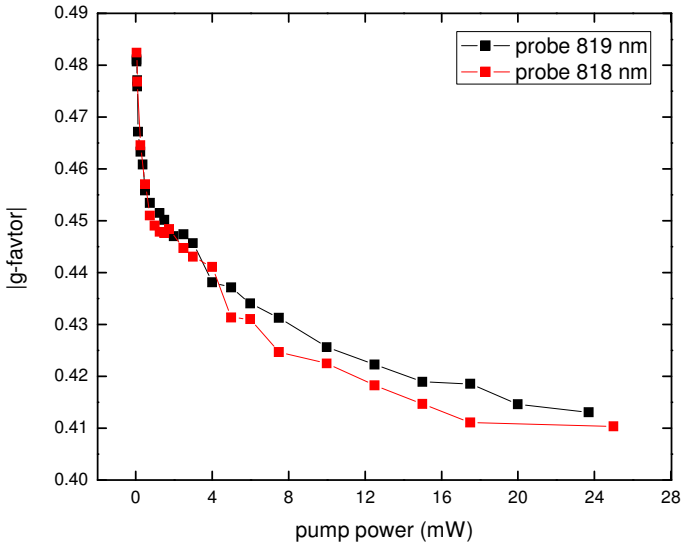

Figure 20 Landé g-factor pump power dependence. Pump pulse was fixed at 814.5 nm. Two different wavelengths of probe we used: 819 nm and 818 nm

4.4.1. Band filling effects

By pumping at higher intensities we were able to study band-filling effects which may explain dynamics of the spin dephasing. When electrons are excited to the conduction band, momentum relaxation occurs. If electrons are excited to the higher levels, they almost rapidly relax to the bottom of the conduction band and fill it up to the quasi Fermi level. As this excited system evolves in time electron-hole recombination takes place and the filling of the conduction band diminishes. Since the g-factor of electrons depends on kinetic energy, the degree of band filling influences spin dynamics and thus spin-dephasing. According to previous studies g-factor linearly depends on kinetic energy of electrons in the band:

$$g(E) = g_0 + aE \tag{4-4}$$

where $g_0 \approx$ -0.44 is a g-factor at the bottom of the conduction band, and a $\approx$ 6.3 eV^{-1} is a constant.

At high intensities (that is the case in this work) an ensemble of electrons with a band of g-factor values, ranging from g_0 to $g(E_f)$, is excited. $E_f \sim N^{2/3}$ is a quasi Fermi

level that is defined by the density of excited electrons. That is why we have to introduce average g-factor for the system.

$$\langle g \rangle = \frac{1}{N} \int_0^{E_f} g(E) \cdot \rho(E) dE \tag{4-5}$$

where $\rho(E) \sim E^{1/2}$ is a three dimensional density of states function. N is a number of excited electrons. After integration we obtain:

$$\langle g \rangle = g_0 + a \cdot k \cdot N^{2/3} \tag{4-6}$$

where $k = (3\pi^2)^{2/3} 3h^2/10m$ is a constant. From (4-6) we can see that the deviation of g-factor from the bottom band value is proportional to the number of electrons excited by laser pulse to the power 2/3, which in its turn is proportional to pump pulse intensity.

If we look at the data of pump-power g-factor dependence (which are extracted from the experimental data, Figure 21) we can distinguish two regions: 1) for low electron densities $N<3\cdot10^{16}$ cm^{-3} there is very steep (nearly exponential) dependence, 2) while for high $N>3\cdot10^{16}$ cm^{-3} g-factor has a power dependence on electron-density. The threshold electron density $N=3\cdot10^{16}$ cm^{-3} appears to be close to the doping level of the active area of our sample. Thus in high intensity regime we observe band filling effects. By fitting high density part of the plot with power function $g(N)=g_0+bN^p$ (Figure 21) we can find the exponent $p=0.49$ which is in a reasonable agreement with the model presented ($p=2/3=0.66$).

Now, if we fix exponent at $p=0.66$ and force it to remain within our model, we can get proportionality constant b and by comparing latter with (4-6) we can get constant a (see equation 4-4). As a result we obtained $a = 1.83$ eV^{-1}. Although it is in quite a disagreement with the results presented in previous works, it does not mean that the whole theory is wrong. This is the result of not being able to determine the diameter of the laser spot on the sample with high precision what resulted in recalculation of the electron densities from pulse power. Estimated diameter of the laser beam at the surface of the sample is 50-100 μm, which only allowed us to get correct order of the proportionality constant a.

Band filling effects result not only in the shift of the average g-factor but also in the decrease of the spin-dephasing time T_2^*, due to spread of the g-factor over the conduction band. Figure 22 shows dependence of spin-dephasing time on pump power.

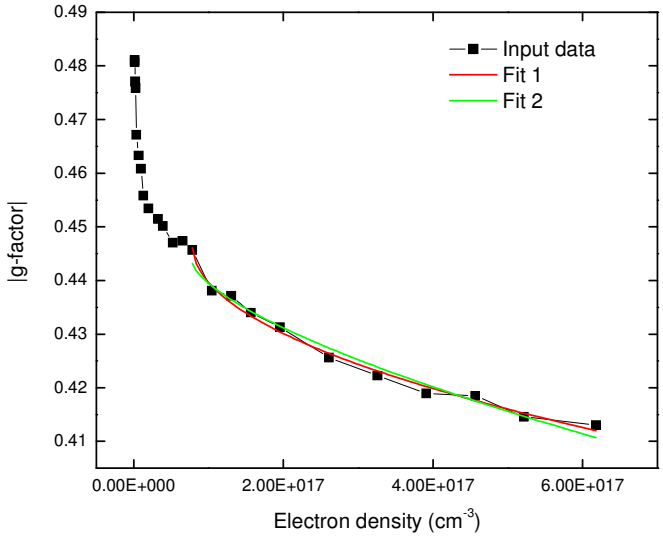

Figure 21 g-factor dependence on the density of excited electrons. Input data are fitted with power function $g(N)=g_0+bN^p$: Fit1: g_0, b and p are free parameters, obtained p = 0.49; Fit 2: p = 0.66 fixed parameter, g_0, b- free parameters.

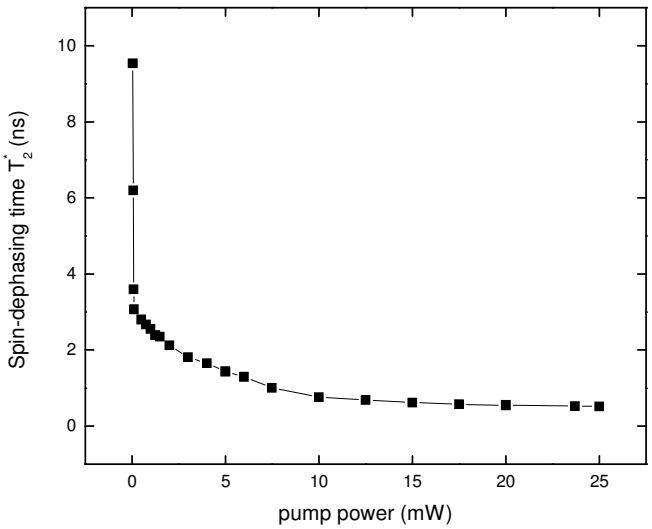

Figure 22 Pump power dependence of the spin dephasing time T_2^* . Pump/probe pulses was fixed at 814.5/819 nm.

Before doing narrow linewidth experiment (with LCF), a similar series of Kerr measurements was performed using wide linewidth (~ 10 nm) laser pulses (without LCF). Also similar result was obtained: Absolute value of the g-factor gradually decreases as

the pump power increases (Figure 23). Non-monotonic dependence of the g-factor on magnetic field is observed. Absolute value of the g-factor is for magnetic field of 4 Tesla is somewhat higher then for 1 and 7 Tesla.

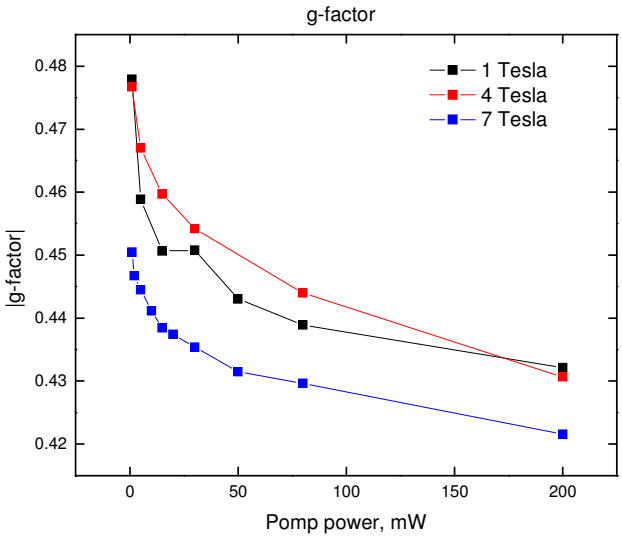

Figure 23 Pump power dependence of the Landé g-factor for different magnetic fields. Mono-colour experiment at $\lambda_{pump} = \lambda_{probe} = 820$ nm for wide spectral line widths (~7 nm) of the pump and probe pulses.

4.4.2. Heating effects

Another factor that may influence spin dynamics of the electron ensemble is heating of the sample by laser beam. Temperature dependence of electron Landé g-factor was studied in [18]. An empirical dependence of the g-factor of temperature is given by:

$$g(T) = -0.44 + 5\times10^{-4}T(K) \tag{4-7}$$

To find out how important heating effects are is our case we have to estimate temperature rise.

If the energy of photon is bigger then the band gap in the semiconductor, electron is excited to the higher levels of the conduction band. Subsequently it relaxes to the unoccupied levels in the bottom of the conduction band. The excess electron energy is transferred to the crystal lattice via scattering with phonons. To estimate temperature rise we have to calculate heat energy injected into the system with one laser pulse and divide in by heat capacity of the crystal. At low temperatures heat in the crystals is carried mainly by phonons and heat capacity is well described by Debye formula [20]:

$$C_v = 234 N_0 k_b \left(\frac{T}{\theta}\right)^3 \tag{4-8}$$

where N_0 is a number of atoms, k_b Boltzmann constant, T temperature, θ is the Debye temperature of the material. After integration over the range of temperatures we can obtain formula for the temperature rise for a laser pulse with particular parameters:

$$T_2 = \left(\varepsilon \cdot P + T_1^4\right)^{1/4} \tag{4-9}$$

where $\varepsilon = (16\Delta E\mu\theta\alpha\lambda)/(117hR\rho cfD)$, $\Delta E=E-E_c$ is electron excess energy, λ f, D are the wavelength, repetition rate and diameter of the laser beam, R - universal gas constant, μ, ρ and α are the molar mass, density and absorption coefficient of the material. Dependence of the temperature rise for typical laser beam power is shown on Figure 24. According to this estimation temperature rise due to the heating from laser pulse remains within 2 K. According to (4-7) this may give maximum deviation of the g-factor $\Delta g \sim 0.001$. Thus heating effects do not essentially influence the results of the experiment (comparing to the band filling effects)

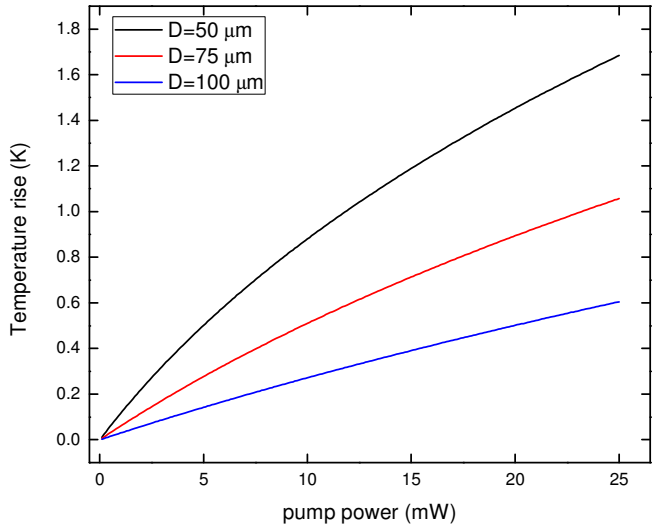

Figure 24 Estimation of the temperature rise due to the electron momentum relaxation within the conduction band. Initial temperature is 4.2 K. Results are given for different diameters of the laser beam D.

5 Conclusions

To summarize, an attempt to answer two questions concerning spin-dephasing processes in GaAs structures was made in this thesis. The first question was to investigate how ballistic confinement of bulk electrons in GaAs effects spin-dephasing time. By performing Monte-Carlo simulations it was shown that confinement indeed effects spin-dephasing, leading to anisotropy of the spin-dephasing time with respect to the wire orientation. An important result is that this anisotropy is present only for certain range of the values of the parameters of the confinement. It was shown that anisotropy disappears if the wire width becomes larger then the spin-precession length. External field dependence of both confined an unconfined 3D spin ensembles was carried out. These simulations also showed that there is also anisotropy with respect to the external field orientation. Thus external magnetic field enhances spin dephasing time more for [110] field orientation then for [-110]

The second part of the thesis dealt with experimental tracing of the spin-relaxation processes in n-doped GaAs sample by employing time resolves Kerr rotation technique. The aim of this part was to find out the origin of the initial phase shift of the Kerr signal, drift of the g-factor and possible relationship between these two processes. It was shown that initial phase shift is a direct consequence of the g-factor drift. And the latter occurs due to conduction electron relaxation processes. Pump power dependence of the electron Landé g-factor studied in this part of the work. Unexpected values of the g-factor were observed for small intensities of the pump beam.

Appendix A

Liquid crystal filter

Tunable liquid crystal filters (LCF) were used for spectral filtering of the pump and probe beams. Part of this thesis work was to install and test these devises in the experimental setup. This appendix presents the results of these tests.

The functioning of the filters is based on the principle of Fabri-Perot interferometer. The transmittance function of the ideal Fabri-Perot etalon is given by:

$$T(\theta,\lambda)=\frac{I(\theta,\lambda)}{I_0(\theta,\lambda)}=\frac{1}{1+(2F/\pi)^2\sin^2(\delta/2)},$$

where $\delta=\frac{4\pi n\cos(\theta)}{\lambda}$, λ is the wavelength of the incoming radiation, d is a plate separation, n is index of refraction of the material between the etalon plates and F is the finesse of the etalon. By tuning either plate separation or refractive index of the material one can tune transmittance function of the etalon. Liquid crystal filters used in our setup used the effect of tuning refractive index by applying voltage to the nematic liquid crystal. The structure of the LCF is shown in Figure A 1. Two silica substrates, each of which has been coated with a transparent indium tin-oxide conductive layer and a reflective mirror, are spin-coated with a polyimide solution and then buffed mechanically. The buffed polyimide layer acts to align the nematic liquid crystal along the buffing direction, parallel to the plane of the substrates.

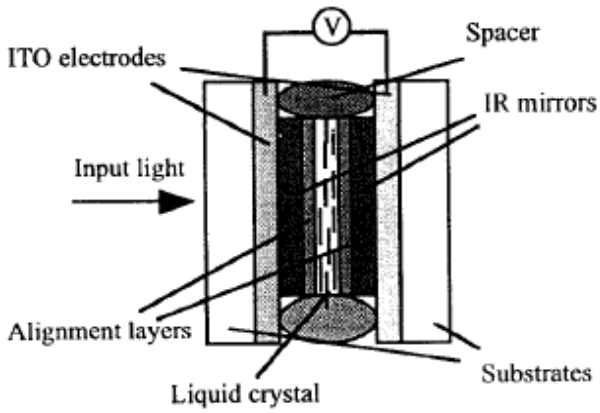

Figure A 1 Schematics of the liquid crystal Fabry-Perot etalon [23]

When an electric field is applied across the cell via the ITO layers, the nematic liquid crystal molecules tend to align with the applied field, thus tilting out of the plane of the substrates. This tilting of the molecules results in a modulation of the birefringence and the optical path length seen by the incoming light. The net result is a tuning of the transmission peaks of the Fabry-Perot etalon.

The main goal of the LCF test was to measure its spectral characteristics, that is line width, finesse, tenability range. For that purpose laser beam was sent through the LCF and the output spectrum was measured recorded by a spectrometer. This was done

for differed voltages applied to filter. In such a way we were able to build a map of the LCF transmission function for a range of applied voltages. A typical dependence of the position of the transmission peaks on the applied voltage is show on Figure A 2. From the plot we can see that this LCF has two tunable peaks in the ranges 782-804 nm and 812-835 nm correspondingly. So the second peak was eligible to produce probe pulse with a wavelength around 820 nm and spectral line width ~1-1.5 mW.

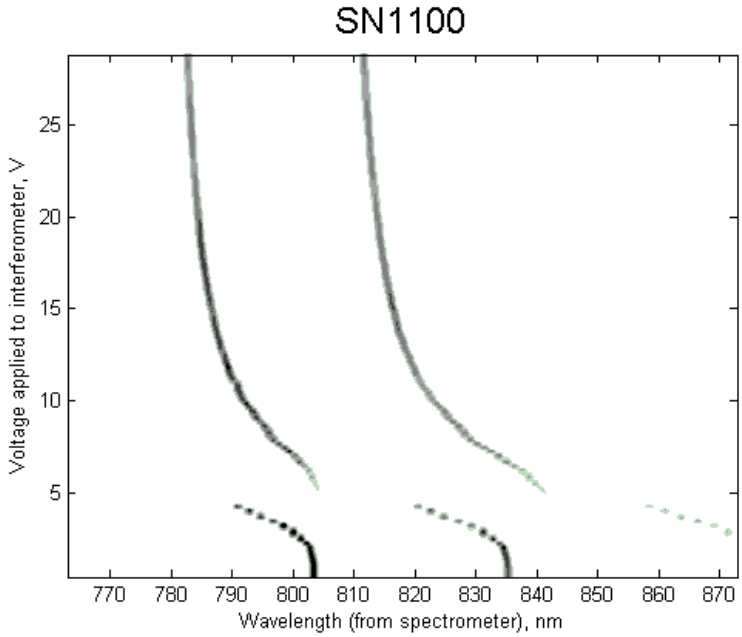

Figure A 2 Dependence of the position of the transmission peaks of the LCF on the applied voltage.

References:

[1] M. N. Baibich *et al*., Phys. Rev. Lett. **61**, 2472 (1988); G. Binasch *et al*., Phys. Rev. B **39**, 4828 (1989).
[2] F. Meier B.P. Zakharchenya, Optical Orientation, (North-Holland Physics, Amsterdam, 1984).
[3] Z. Q. Qiu *et al*., Rev. Sci. Instrum. **71**, 1243 (2000).
[4] R. H. Silsbee, J. Phys.: Condens. Matter **16**, R179 (2004).
[5] J. Liu *et al*., arXiv:0810.1413.
[6] S. Z. Denega *et al.*, preprint (Univ. of Groningen, 2008).
[7] A.W. Holleitner *et al.*, Phys. Rev. Lett **97**, 036805 (2006).
[8] J. B. Miller *et al.*, Phys. Rev. Lett. **90**, 076807 (2003).
[9] B. Andrei Bernevig *et al.*, Phys. Rev. Lett., **97**, 236611 (2006).
[10] T. Korn *et al*., Physica E **40** 1542 (2008).
[11] J. M. Kikkawa, *et al*., Phys. Rev. Lett. **80**, 4313 (1998).
[12] R. I. Dzhioev, *et al*., Phys. Rev. B **66**, 245204 (2002).
[13] A. I. Ekimov, *et al*., Pis'ma Zh. Eksp. Teor. Fiz. **13**, 251–254 [JETP Lett. **13**, 177–179 (1971)].
[14] R. I. Dzhioev, *et al*., Phys. Solid State **39**, 1765–1768 (1997).
[15] Available at http://www.nd.edu/~gsnider/
[16] J. S. Colton *et al.*, Phys. Status Solidi B **233**, 455 (2002).
[17] C. Weisbuch *et al*., Phys.Rev. B **15**, 816 (1977); P. E. Hohage *et at*., Appl. Phys. Lett. 89, 231101 (2006).
[18] M. Oestreich, *et al*., Phys. Rev, B **53**, 7911 (1996).
[19] J. Hübner, *et al*., Phys. Rev. B **79**, 193307 (2009).
[20] Kittel Charles, Introduction to Solid State Physics, 8th Edition.
[21] Bennett, Jean M . "Polarizers". in Bass, Michael, Ed.. Handbook of Optics Volume II.
[22] D. Paget *et al.*, Phys. Rev. B **15**, 5780 (1977).
[23] Morita, Y *et al.*, 10.1109/LEOSST.1996.540709.